ISSN 1029-9599, Physical Mesomechanics, 2013, Vol. 16, No. 2, pp. 125–132 © Pleiades Publishing, Ltd., 2013.
Original Russian Text © S.P. Kiselev, E.V. Zhirov, 2012, published in Fizicheskaya Mezomekhanika, 2012, Vol. 15, No. 2, pp. 69–76.

Molecular Dynamics Simulation of Deformation and Fracture of Graphene under Uniaxial Tension

S. P. Kiselev* and E. V. Zhirov

Khristianovich Institute of Theoretical and Applied Mechanics, Siberian Branch, Russian Academy of Sciences, Novosibirsk, 630090 Russia
** kiselev@itam.nsc.ru*

Received Jule 27, 2011

Abstract—The paper reports on molecular dynamics simulation of deformation and fracture of graphene under uniaxial tension. Dependences of Young's modulus, critical force and fracture strain on the strain rate, temperature and angle between the tension direction and the graphene lattice are derived. The effect of defects on fracture of graphene is studied.

DOI: 10.1134/S1029959913020033

Keywords: graphene, molecular dynamics, defects, strain, fracture.

1. INTRODUCTION

Graphene is a monolayer of carbon atoms with a hexagonal two-dimensional structure. It can be represented as a graphite plane separated from the bulk crystal. Graphene was discovered in 2004 and at the moment its properties are intensively studied, both experimentally and theoretically [1–5]. The experiments show that graphene possesses unique electronic and mechanical properties. In particular, it has high mechanical stiffness (Young's modulus E is about 1 TPa) and good thermal conductivity (thermal conductivity coefficient is about 5×10^3 W/(m·K). High mobility of charge carriers makes it a promising material for future use in various applications, in particular, in nanoelectronics and in integrated circuits instead of silicon.

Paper [1] presents the atomic force microscopy results on perforation of circular graphene membranes suspended on a silicon substrate. Assuming the graphene sheet to be 0.335 nm thick, the Young's modulus is found to be 1.0 ± 0.1 TPa. In addition, the critical fracture stress is 130 ± 10 GPa, that at the given sheet thickness corresponds to the force 42 ± 4 N/m. Note that the experiments for graphite give a similar Young's modulus of 1.02 ± 0.03 TPa.

Papers [2, 3] demonstrate the results of numerical simulation of deformation and fracture of a graphene sheet using quantum mechanical calculation of electron density. The following characteristics of graphene are obtained: Young's modulus 1.0 TPa and fracture force 43 N/m. Tension is performed by successive displacements of edge atoms with the intermediate relaxation of the system at zero temperature up to fracture. The electron density functional method is used in [4] to obtain the following graphene characteristics: Young's modulus 1.05 TPa, Poisson's ratio 0.186, and critical stress fracture 110 GPa (36.85 N/m) in the "armchair" direction and 121 GPa (40.54 N/m) in the "zigzag" direction.

Paper [5] conducts the molecular dynamics simulation of deformation and fracture of graphene using LAMMPS [6]. The interaction between carbon atoms is calculated using the AIREBO potential [7]. The following characteristics are obtained: Young's modulus 1.01 ± 0.03 TPa, Poisson's ratio 0.21 ± 0.01, and critical stress fracture 90 GPa (30 N/m) in the "armchair" direction and 107 GPa (36 N/m) in the "zigzag" direction. Here tension is also carried out by successive displacements of edge atoms with the intermediate relaxation of the system. The strain rate of graphene is $0.001/\text{ps} = 10^9\ \text{s}^{-1}$ and temperature is 300 K.

Mentioned papers [2–5] pay special attention to the study of the influence of the graphene sheet boundary on its strength properties. Consideration is given to free surfaces of graphene such as "armchair" and "zigzag" as well as to the case of an "infinite" sheet simulated by pe-

riodic boundary conditions. The strength of a graphene sheet with the free "zigzag" boundary is higher than that of graphene with the "armchair" boundary and is close to the "infinite" sheet strength.

This paper examines how mechanical properties of graphene are affected by strain rate, temperature, and defects at the boundary and surface of the graphene sheet.

2. CALCULATIONAL PROCEDURE

2.1. Molecular dynamics method

Deformation and fracture of graphene was simulated by the molecular dynamics method. All calculations are made in the LAMMPS software [6]. The molecular dynamics method consists in the numerical integration of the equations of motion

$$\dot{p}_j = -\frac{\partial H}{\partial x_j}, \quad \dot{x}_j = -\frac{\partial H}{\partial p_j}, \tag{1}$$

where H is the complete Hamiltonian of the system, p_j is the momentum, and x_j is the coordinate.

Graphene is kept at a constant temperature using the Berendsen thermostat and direct scaling of velocities [8]. The Berendsen algorithm is based on the introduction of alternating friction. Deviation of temperature T from its equilibrium value T_0 is corrected according to the equation $\mathrm{d}T(t)/\mathrm{d}t = (T_0 - T(t))/\tau$. The Berendsen thermostat is known to be weak for relatively small systems (up to a hundred of atoms) and long bond lengths due to nonuniform energy distribution over degrees of freedom. This problem does not arise in the given case as the system has about a thousand of atoms and bond lengths of particles are localized near lattice sites. The initial temperature is introduced by setting the thermal velocity of atoms according to the Maxwell distribution.

2.2. Choice of the potential

Hamiltonian H entering (1) is the sum of kinetic and potential energy of atom interaction (the potential). The given paper tests the following potentials: MEAM [9], Tersoff [10], and AIREBO [7].

MEAM [9] is the most universal potential. Parameterization is available for the large part of the periodic table. However, the test calculations show that the MEAM potential describes graphene poorly. In this case the hexagonal structure is unstable even at low temperatures.

The Tersoff potential [10] is developed to describe short-range covalent bonds of silicon and carbon atoms. However, the test calculations show that it proposes the improbable description of graphene behavior under tension. The numerical calculation performed by the Tersoff potential causes the lateral expansion of graphene under longitudinal tension (negative Poisson's ratio).

The AIREBO potential [7] is created to simulate complex processes (including chemical reactions) with hydrocarbons. This potential also provides a possibility to simulate the carbon–hydrogen interaction. The potential consists of the three parts

$$E = \frac{1}{2}\sum_i \sum_{j\neq i}\left[E_{ij}^{\mathrm{REBO}} + E_{ij}^{\mathrm{LJ}} + \sum_{k\neq i,j}\sum_{l\neq i,j,k} E_{kijl}^{\mathrm{t}} \right], \tag{2}$$

where $E_{ij}^{\mathrm{REBO}} = V_{ij}^{\mathrm{R}} + b_{ij}V_{ij}^{\mathrm{A}}$ is the REBO potential that is of a Tersoff type and describes short-range covalent bonds in carbon atoms. Here V_{ij}^{R} is the repulsive term, V_{ij}^{A} is the attractive term, and b_{ij} is the angle-dependent factor of proportionality. The repulsive term in (2) has the form $V_{ij}^{\mathrm{R}} = w_{ij}(r_{ij})\left[1 + Q_{ij}/r_{ij}\right]A_j e^{-\alpha_{ij}r_{ij}}$, where Q_{ij}, A_{ij}, and α_{ij} depend on types of interacting atoms i and j. The cutoff function $w_{ij} = w_{ij}(r)$ ensures the smooth elimination of the REBO part on achieving the maximum range of action and has the form [7]

$$w_{ij} = \begin{cases} 1, & r_{ij} < r_{\mathrm{c}}, \\ 0.5(1+\cos(\pi(r_{ij} - r_{\mathrm{c}})/\Delta)), & r_{\mathrm{c}} \le r_{ij} < r_{\mathrm{c}} + \Delta, \\ 0, & r_{ij} \ge r_{\mathrm{c}} + \Delta, \end{cases} \tag{3}$$

where r_{c} is the cutoff radius and Δ is the width of "smearing" of the cutoff function $w_{ij} = w_{ij}(r)$. The attractive term in (2) has the form $V_{ij}^{\mathrm{A}} = -w_{ij}(r_{ij})\sum_{n=1}^{3} B_{ij}^n e^{-\beta_{ij}^n r_{ij}}$, where B_{ij} and β_{ij} also depend on atom types. Potential E^{LJ} is the potential of a Lennard-Jones type, which describes the long-range interaction and is represented as

$$V_{ij}^{\mathrm{A}} = \breve{s}_{ij}(r_{ij})C_{ij}V_{ij}^{\mathrm{LJ}}(r_{ij}) + (1 - \hat{s}(r_{ij}))C_{ij}V_{ij}^{\mathrm{LJ}}(r_{ij}), \tag{4}$$

$$V_{ij}^{\mathrm{LJ}} = 4\varepsilon_{ij}(r_{ij})\left[\left(\frac{\sigma_{ij}}{r_{ij}}\right)^{12} - \left(\frac{\sigma_{ij}}{r_{ij}}\right)^{6}\right],$$

where $\breve{s}_{ij}$, $\hat{s}$, and C_{ij} are the cutoff functions and V_{ij}^{LJ} is the classical Lennard-Jones potential. Potential E^{t} in (2) describes the torsional potential about bonds:

$$E_{ijkl}^{\mathrm{t}} = w_{ij}(r_{ij})w_{ik}(r_{ik})w_{jl}(r_{jl})V^{\mathrm{t}}(\omega_{ijkl}), \tag{5}$$

$$V^{\mathrm{t}} = \frac{256}{405}e_{ijkl}\cos^{10}(\omega_{ijkl}/2) - \frac{1}{10}e_{ijkl}.$$

Numerical values in (2)–(5) for the AIREBO coefficients are given in [7], the cutoff radius comprises 0.2 nm for the REBO part and 1.02 nm for the LJ part. The choice of the cutoff radius for the REBO potential will be further discussed.

2.3. Numerical experiments

The original software is used to prepare molecular configurations of graphene sheets about 5 nm in size and with a required lattice angle. Atoms located on the upper and lower edges (Fig. 1) are excluded from the calculation in the tension direction. Though subjected to no longitudinal forces, these atoms affect neighboring atoms in the computational region. These atoms can move in the transverse direction under the action of neighboring atoms located in the computational region. The lower edge remains stationary while atoms in the upper edge are specified to shift continuously and slowly at each step. The tensile velocity for the upper edge is about 10 m/s, which corresponds to the strain rate $v/l = 10^9$ s^{-1}, where v is the tensile velocity, l is the characteristic size of the system (in this paper l is the initial longitudinal size of the graphene sheet and equals 5 nm in all experiments). The two side edges remain free or periodic boundary conditions are set on them.

Before each numerical experiment the system is optimized and is gradually brought to the desired temperature using the thermostat. The typical molecular configuration of the completely optimized system is shown in Fig. 1. Tension proceeds until fracture. In this paper fracture is assumed to occur at the moment when average stress in the specimen drops to zero.

2.4. Calculation of mechanical parameters of graphene

The following parameters are calculated for graphene: Young's modulus, critical fracture stress F_*, and corresponding fracture strain ε_*. Graphene strain along the tension axis Oy is calculated by the formula

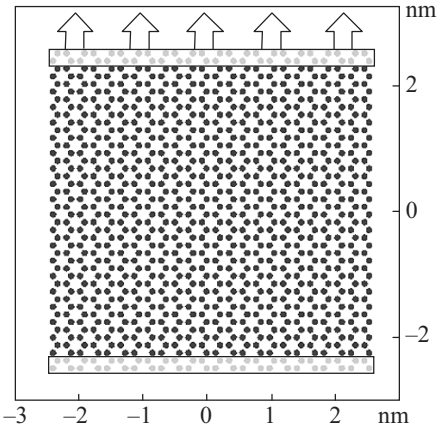

Fig. 1. Molecular configuration of "zigzag" graphene before tension. Arrows indicate the tension direction.

$$\varepsilon_y = \frac{l - l^0}{l^0}, \tag{6}$$

where l is the current size of the plate in the tension direction and l^0 is the initial size in the same direction.

Stress in the graphene sheet is calculated in the following way. First the symmetric stress tensor for each atom is found by the formula

$$S_{ij} = -\frac{1}{V_a}\left(m v_i v_j + \frac{1}{2}\sum_{n=1}^{N_p} (r_{1i}F_{1j} + r_{2i}F_{2j}) \right), \tag{7}$$

where V_a is the volume occupied by a carbon atom in graphene. The first term in formula (7) is the kinetic energy contribution for an atom, the second term is the pairwise energy contribution for N_p neighbors of the given atom, r_1 and r_2 are the coordinates of the two atoms in pairwise interaction, F_1 and F_2 are the forces on the two atoms resulting from pairwise interaction. Then the specific longitudinal force $F = F_f/a$ is calculated per unit lateral dimension of the plate by the formula

$$F = \frac{1}{a}\sum_N \frac{ah}{N} S_{yy} = \frac{V}{Nab}\sum_N S_{yy}, \tag{8}$$

where $V = abh$ is the volume occupied by the graphene sheet, a is the lateral dimension, b is the longitudinal dimension, h is the graphene thickness, and ah/N is the cross sectional area per carbon atom. Formulae (7) and (8) are used to plot tension diagrams expressing the dependence of specific force on relative elongation.

Young's modulus is defined by the formula

$$E = \frac{1}{S}\frac{dF_f}{d\varepsilon_y} = \frac{1}{h}\frac{dF}{d\varepsilon_y}, \tag{9}$$

where F_f is the total longitudinal force in the specimen and $S = ah$ is the cross sectional area of the graphene sheet. Force F is deduced by formula (8), the derivative in formula (9) is calculated providing $\varepsilon_y \to 0$. The graphene sheet thickness $h = 0.335$ nm is chosen similarly to paper [5].

In numerical tensile experiments critical force F_* and critical fracture strain ε_* are taken immediately before graphene fracture (fracture moment $t = t_*$ is defined at $F = 0$). This corresponds to the maximum force in the tension diagrams $F(\varepsilon)$. Here and below we omit the strain component subscript $\varepsilon = \varepsilon_y$ for brevity sake.

3. NUMERICAL RESULTS

The above-described procedure is used to conduct numerical experiments with cutoff parameters chosen in the AIREBO potential and to study graphene fracture in relation to temperature, strain rate, angle between the

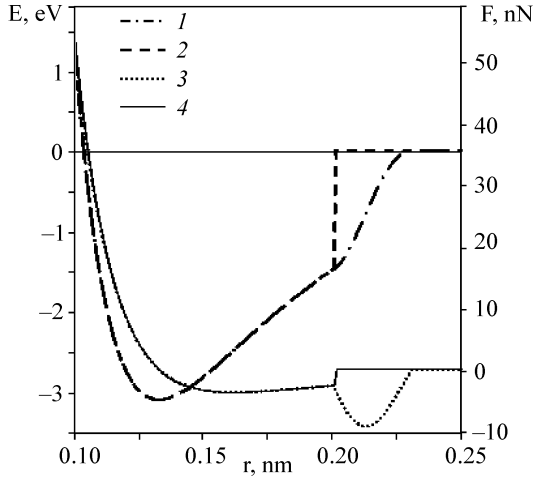

Fig. 2. Potential energy E (*1*, *2*) and interaction force F (*3*, *4*) versus length r between two carbon atoms for the cutoff radius $r_c = 0.2$ nm at different "smearing" width $\Delta = 0.03$ (*1*, *3*) and 0.001 nm (*2*, *4*). E = 2.0–2.3 (*1*), 2.00–2.01 (*2*), F = 2.0–2.3 (*3*), 2.00–2.01 (*4*).

tension direction and lattice orientation, and boundary and surface defects.

3.1. Choice of the cutoff radius in the AIREBO potential

For the AIREBO potential the cutoff radius in formula (3) is first proposed to equal $r_c = 0.17$ nm [7]. Paper [11] points to the fact that for tensile problems the cutoff radius in formula (3) should be increased to $r_c = 0.2$ nm. As noted in [12], at the cutoff point $r_{ij} = r_c$ there is a jump in the potential derivative $\partial E/\partial r_{ij}$, that leads to a nonphysical increase in the attractive force between carbon atoms $F_{ij} = -\partial E/\partial r_{ij}$. Subsequent papers use the cutoff radius $r_c = 0.2$ nm and however they lack the information on how the interaction force is affected by the "smearing" width Δ of cutoff function (3). Figure 2 demonstrates the dependence of potential energy and interaction force between two carbon atoms, which is calculated at the same cutoff radius $r_c = 0.2$ nm but for different "smearing" widths $\Delta = 0.001$ and 0.03 nm. At $r_c < r < r_c + \Delta$ a nonphysical attractive force is seen to arise between carbon atoms for $\Delta = 0.03$ nm while there is no such force for $\Delta = 0.001$ nm. Figure 3 exhibits strain dependences $F(\varepsilon)$ of specific force, which are built under tension of graphene at different values of r_c and $r_c + \Delta$. The calculations are performed at the graphene temperature 300 K, tensile velocity 100 m/s, and with free side "zigzag" boundaries. In the range of the cutoff radius from 0.19 to 0.21 nm critical specific force F_* and strain ε_* are seen to depend sufficiently on the "smearing" width Δ. From the comparison of our calculation results (Fig. 3) and the results of mentioned papers [2–5] follows that the AIREBO potential requires the cutoff radius 0.19 nm < r_c < 0.21 nm and "smearing" width $0 \le \Delta < 0.001$ nm in formula (3).

3.2. Graphene fracture affected by strain rate and temperature

Figure 4 illustrates tension diagrams $F(\varepsilon)$ for graphene calculated at different strain rates $\dot{\varepsilon} = v/b$, where tensile velocities v are mentioned in Fig. 4. Strain rate is seen to have a weak influence on critical fracture parameters. This is explained by the fact that before fracture graphene is deformed as a nonlinear elastic solid. A slight growth in critical force $\Delta F_*/F_* \approx 0.05$ with a 10^3-fold increase in strain rate is related to the finite frac-

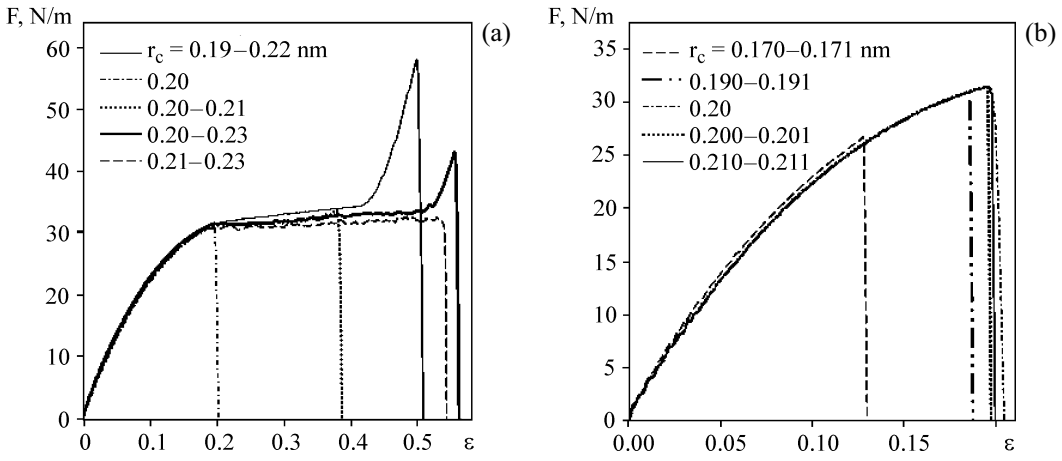

Fig. 3. Specific force versus strain $F(\varepsilon)$ in tension of graphene for different cutoff radii r_c at 0 nm ≤ Δ ≤ 0.03 nm (a) and 0 nm ≤ Δ ≤ 0.001 nm (b).

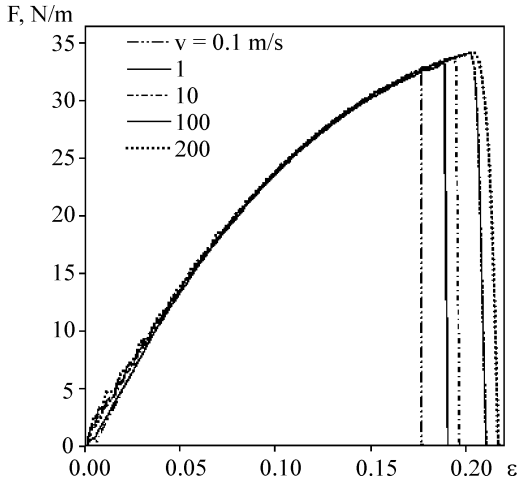

Fig. 4. Dependence $F(\varepsilon)$ in tension of graphene (periodic boundary conditions at the side boundaries) at different tensile velocities.

ture time of graphene. The following mechanical parameters of graphene are derived in Fig. 4: Young's modulus (9) $E = 0.96 \pm 0.05$ TPa, critical force $F_* = 34$ N/m, and critical fracture strain $\varepsilon_* \approx 0.2$. The experimental values of Young's modulus, critical force, and strain are [1] 1.02 ± 0.03 TPa, 42 ± 4 N/m, and 0.25, respectively. Critical fracture force is seen to be underestimated by 20% in the numerical calculations by the AIREBO potential while the rest calculated parameters are close to the experimental values.

Figure 5 depicts calculated values for deformation of the graphene sheet with the "zigzag" boundary at different temperatures. With growing temperature critical force and fracture strain of the graphene sheet is observed to decrease continuously. At a temperature more than 2 000 K the graphene sheet looses its stability and fractures under arbitrary small loads.

3.3. Graphene fracture affected by boundary and surface defects

Papers [2–5] demonstrate that critical fracture parameters F_* and ε_* are reduced considerably as the side boundary of the graphene sheet changes its type from "zigzag" to "armchair". In both limiting cases the graphene sheet consists of hexagons and lacks defects. Of interest is to study tension of the graphene sheet at the arbitrary orientation of its boundary relatively to the tension axis. With consideration for the graphene lattice symmetry the angle $\alpha = 0°$ corresponds to the "zigzag" boundary while the angle $\alpha = 30°$ to the "armchair" boundary. For intermediate angles the graphene sheet boundary contains defects in the form of incomplete hexagons. Figure 6a presents the calculation results for $F(\varepsilon)$ at different angles of lattice orientation with respect to the tension axis. Critical parameters are maximum for the "zigzag" boundary. Circles connected by a line in Fig. 6a demonstrate the $F(\varepsilon)$ dependence calculated in paper [5] at the strain rate $\dot{\varepsilon} = 10^9$ s^{-1} for the AIREBO potential by the LAMMPS software [6]. The results for the "zigzag" boundary obtained in the present paper are in good agreement with those obtained in paper [5]. In contrast to [5], the present paper studied graphene sheet boundaries intermediate between the "armchair" and "zigzag" types. Even a small angle of rotation by $\alpha = 3°$ relatively to the "zigzag" direction results in a considerable decrease in critical fracture parameters F_* and ε_*. This is associated with the presence of defects of an in-

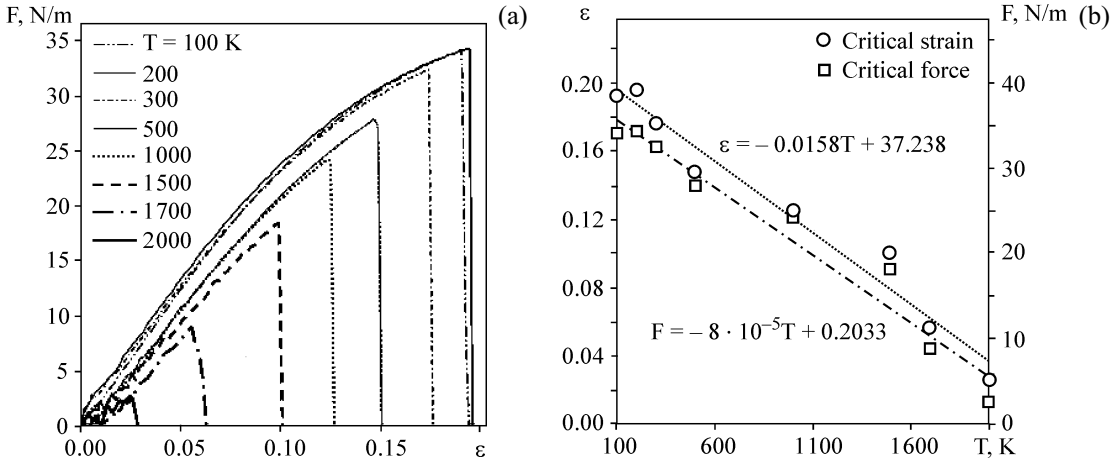

Fig. 5. Dependences $F(\varepsilon)$ in tension of graphene (boundary conditions at the "zigzag" side boundaries) at different temperatures (a); critical specific force and fracture strain versus temperature (b).

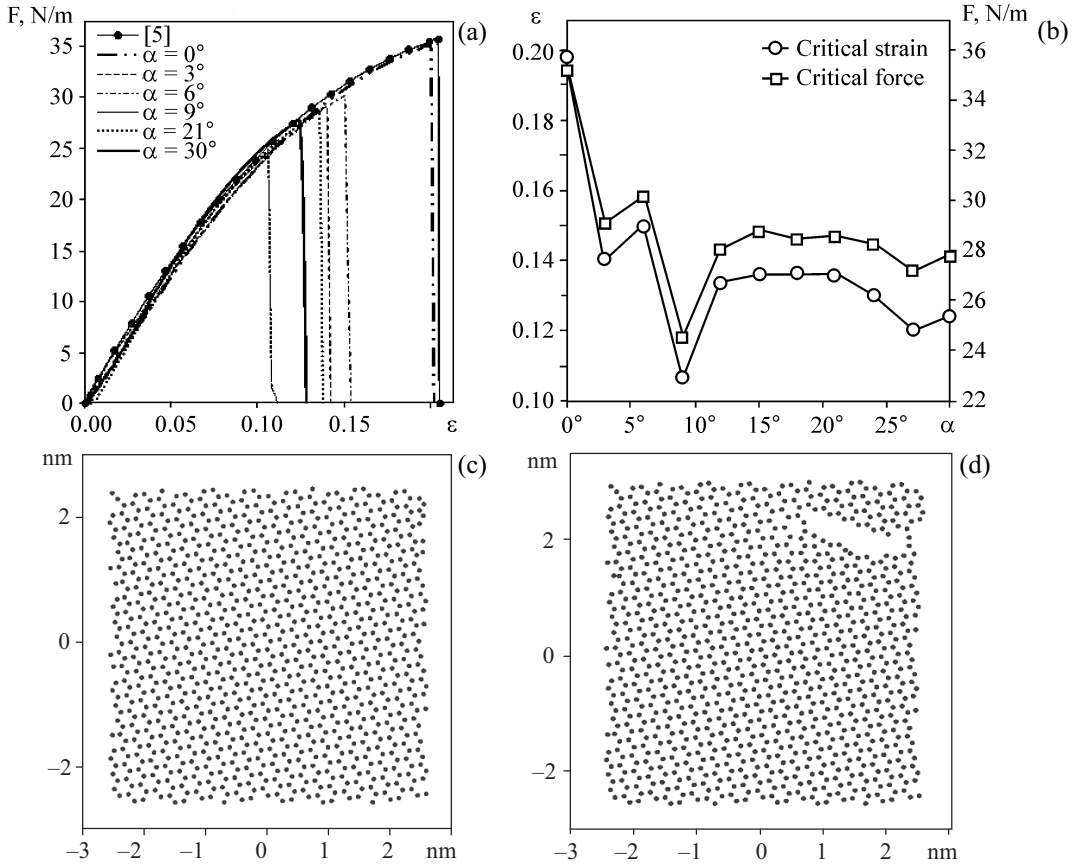

Fig. 6. Dependence $F(\varepsilon)$ in tension of graphene at different angles α (a); critical specific force F_* and fracture strain ε_* versus angle α (b); molecular configuration of graphene with the angle $\alpha = 9°$ before tension (c) and before fracture (d).

complete hexagon type at the boundary, which reduce the energy of pore and crack initiation at the boundary. Paper [13] shows that the edge energy decreases continuously with increasing angle from "zigzag" to "armchair". This should lead to a continuous decrease in critical stress and fracture strain of graphene. These calculation results (Fig. 6b) illustrate that with increasing angle F_* and ε_* decrease and however their angle dependence is not a monotone function. This difference is related to the fact that paper [13] studies chiral angles with the complete periods (m, n), when the boundary consists of regular hexagons. In this case tension is simulated with arbitrary angles and therefore the boundary consists of incomplete hexagons (Fig. 6c, $\alpha = 9°$), on which a crack is generated (Fig. 6d, $\alpha = 9°$). The edge energy is determined not only by the number of hexagons at the boundary but also by the degree of their completion. For all considered angles (except for $\alpha = 9°$) critical values are between those for the "armchair" boundary ($\alpha = 30°$) $F_* = 27.2$ N/m and $\varepsilon_* = 0.128$ and for the "zigzag" boundary ($\alpha = 0°$) $F_* = 35$ N/m and $\varepsilon_* = 0.2$. Note that in paper [5] close critical values are obtained for stress and strain for the "zigzag" boundary $F_* = 36$ N/m and $\varepsilon_* = 0.2$ and for the "armchair" boundary $F_* = 30.2$ N/m and $\varepsilon_* = 0.13$.

Besides the considered boundary defects, the graphene sheet can have surface defects. Figure 7 exhibits

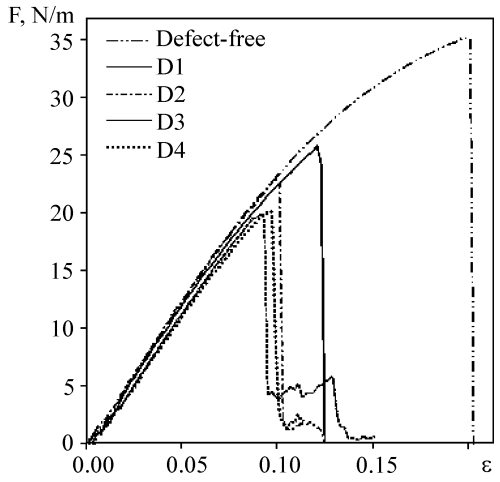

Fig. 7. Dependence $F(\varepsilon)$ in tension of graphene with different defect types.

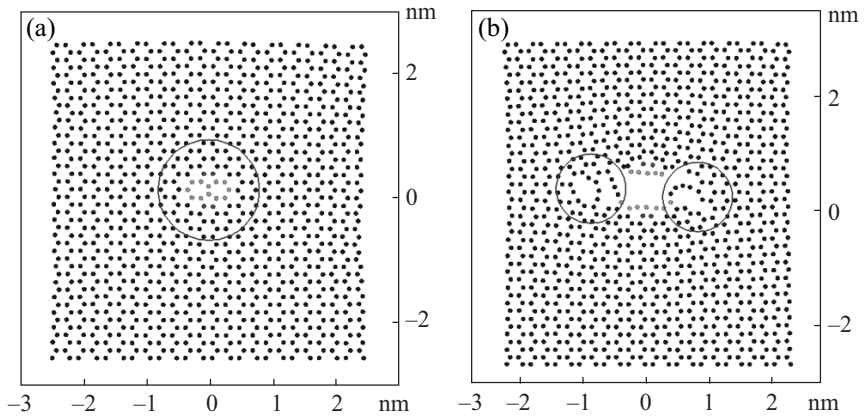

Fig. 8. Molecular configuration of graphene with defect D_1 (marked by a circle) before tension (a) and molecular configuration of graphene with defect D_1 before fracture (crack tips are circled) (b).

calculated dependences $F(\varepsilon)$ for the four defect types $D_1 - D_4$. Defect D_1 is formed due to two carbon atoms shifted from corners of two hexagons to two neighboring hexagons. This leads to the formation of two heptagons and two pentagons within a circle marked in Fig. 8a. Defect D_2 presents a pore formed by the elimination of two carbon atoms (Fig. 9a), defect D_3 is a pore formed by the elimination of four carbon atoms, and defect D_4 (Fig. 9c) is formed of two D_3 pores. Defects are formed at zero temperature and then the defected graphene sheet is heated to 300 K. The graphene sheet measures 5×5 nm, boundary is of a "zigzag" type. In tension of the graphene sheet with the only defect D_1 there is a considerable decrease in critical fracture parameters (Fig. 7). For the graphene sheet with defects $D_2 - D_4$ critical fracture values are close and less than those for defect

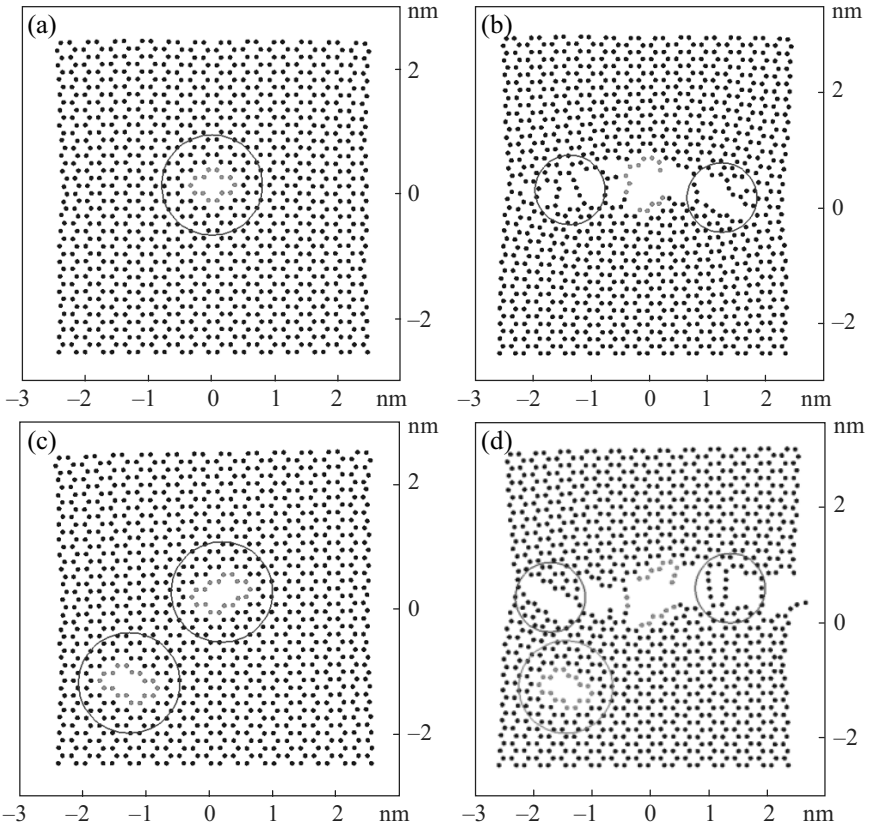

Fig. 9. Molecular configuration of graphene with defect D_2 (marked by a circle) before tension (a); molecular configuration of graphene with defect D_2 before fracture (crack tips are circled) (b); molecular configuration of graphene with defect D_4 (marked by two circles) before tension (c); molecular configuration of graphene with defect D_4 before fracture (crack tips are circled) (d).

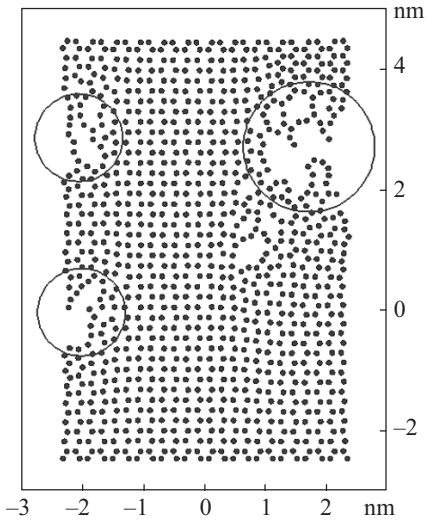

Fig. 10. Molecular configuration of defect-free graphene (crack tips are circled).

D_1. Such behavior of graphene is related to the fact that the presence of a pore decreases much more the crack initiation energy than defect D_1. Fracture of defected graphene is nucleated in the vicinity of defects and proceeds due to crack propagation in the direction perpendicular to the tension axis (Fig. 8b, 9b). Fracture of defect D_4 formed of two pores is peculiar. A transverse crack is initiated near a defect placed in the graphene sheet center. Elastic relief at the crack results in a stress decrease in the graphene sheet and therefore the second defect remains unchanged and exerts no influence on fracture. For a defect-free graphene sheet cracks are initiated at the boundary and propagate within the sheet at an angle of 45° to the tension axis (Fig. 10).

4. CONCLUSION

The given calculation results show that the molecular dynamics method with the AIREBO potential at well-chosen cutoff parameters describes well the graphene behavior under uniaxial tension in the graphene sheet plane. Tension in graphene occurs similarly to that in a two-dimensional nonlinear elastic body. Fracture of graphene is brittle, which explains the weak influence of stress and fracture strain on tensile velocity in a wide range. A temperature increase leads to a continuous decrease in critical stress and strain. The obtained critical values of stress and strain for "defect-free" graphene depend on the structure of the free surface of the graphene sheet ("armchair", "zigzag") and agree with the available literature data. Fracture sites of "defect-free" graphene are generated at the boundary and propagate within the graphene sheet. Surface and boundary defects in graphene reduce considerably the critical stress and fracture strain. Fracture sites of defected graphene are initiated from defects and propagate transversely to the tension axis. As real graphene specimens contain defects, the derived critical values of stress and strain for defected graphene can be useful for graphene investigation.

The work is performed at partial financial support of RFBR grant no. 11-01-00357.

REFERENCES

1. Lee, C., Wei, X., Kysar, J.W., and Hone, J., Measurements of the Elastic Properties and Intrinsic Strength of Monolayer Graphene, *Science*, 2008, vol. 321, pp. 385–388.
2. Yanovskii, Yu.G., Nikitina, E.A., Karnet, Yu.N., and Nikitin, S.M., Quantum Mechanics Study of the Mechanism of Deformation and Fracture of Graphene, *Phys. Mesomech.*, 2009, vol. 12, no. 5–6, pp. 254–262.
3. Yanovskii, Yu.G., Nikitina, E.A., Karnet, Yu.N., and Nikitin, S.M., Simulation of Deformation and Fracture of Graphene: Effect of Size, Defects and Surface Modification, *Phys. Mesomech.*, 2010, vol. 13, no. 5–6, pp. 329–336.
4. Liu, F., Ming, P., and Li, J., Ab Initio Calculation of Ideal Strength and Phonon Instability of Graphene under Tension, *Phys. Rev. B.*, 2007, vol. 76, pp. 064120–064120-7.
5. Zhao, H., Min, K., and Aluru, N.R., Size and Chirality Dependent Elastic Properties of Graphene Nanoribbons under Uniaxial Tension, *Nano Letters*, 2009, vol. 9, no. 8, pp. 3012–3015.
6. Plimpton, S.J., Fast Parallel Algorithms for Short-Range Molecular Dynamics, *J. Comput. Phys.*, 1995, vol. 117, pp. 1–9.
7. Stuart, S.J., Tutein, A.B., and Harrison, J.A. Areactive Potential for Hydrocarbon with Intermolecular Interactions, *J. Chem. Phys.*, 2000, vol. 112, pp. 6472–6486.
8. Berendsen, H.J.C., Postma, J.P.M., van Gunsteren, W.F., DiNola, A., and Haak J.R., Molecular-Dynamics with Coupling to an External Bath, *J. Chem. Phys.,* 1984, vol. 81, no. 8, pp. 3684–3690.
9. Baskes, M., Modified Embedded-Atom Potentials for Cubic Materials and Empurities, *Phys. Rev. B.*, 1992, vol. 46, pp. 2727–2742.
10. Tersoff, J., Modeling Solid-State Chemistry: Interatomic Potentials for Multicomponent Systems, *Phys. Rev. B.*, 1989, vol. 39, no. 8, pp. 5566–5568.
11. Shenderova, O.A., Brenner, D.W., Omeltchenko, A., Su, X., and Yang, L.H., Atomistic Modeling of the Fracture of Polycrystalline Diamond, *Phys. Rev. B.*, 2000, vol. 61, no. 6, pp. 3877–3888.
12. Belytschko, T., Xiao, S.P., Schatz, G.C., Su, X., and Ruoff, R.S., Atomistic Simulations of Nanotube Fracture, *Phys. Rev. B.*, 2002, vol. 65, pp. 235430–235430-8.
13. Gan, C.K. and Srolovitz, D.J., First Principles Study of Graphene Edge Properties and Flake Shapes, *Phys. Rev. B.*, 2010, vol. 81, pp. 125445–125445-8.